Research Square

Preprints are preliminary reports that have not undergone peer review.
They should not be considered conclusive, used to inform clinical practice,
or referenced by the media as validated information.

Protein Quality Control Failure Enables Toxic Gain-of-Function by TDP43 C-Terminal Fragments

Winnie M. Mirembe
Texas Woman's University
Kanchan Budhathoki
Texas Woman's University
Yasar Arfat T Kasu
Texas Woman's University
Kimberly Castro
Texas Woman's University
Serina Patel
Texas Woman's University
Elaina Hildner
Texas Woman's University
Elisa Na
Texas Woman's University
Christopher S. Brower
cbrower@twu.edu
Texas Woman's University

Research Article

Keywords: aggregation, amyotrophic lateral sclerosis (ALS) (Lou Gehrig disease), frontal temporal lobar degeneration (FTLD), proteasome, TAR DNA-binding protein 43 (TDP-43) (TARDBP), pre-mRNA splicing, Stathmin-2

Posted Date: March 5th, 2026

DOI: https://doi.org/10.21203/rs.3.rs-8921356/v1

License: This work is licensed under a Creative Commons Attribution 4.0 International License.
Read Full License

Additional Declarations: No competing interests reported.

Protein Quality Control Failure Enables Toxic Gain-of-Function by TDP43 C-Terminal Fragments

Winnie M. Mirembe, Kanchan Budhathoki, Yasar Arfat T. Kasu, Kimberly Castro, Serina Patel, Elaina Hildner, Elisa Na, and Christopher S. Brower

From the Department of Biology, Texas Woman's University, Denton, TX 76204, USA

Country affiliation for all authors: United States of America

Short title: Toxicity associated with TDP43 C-terminal fragments

To whom correspondence should be addressed: Christopher Brower, Division of Biology, Texas Woman's University, Denton, TX 76204-5799, Telephone: (940) 898-2706; E-mail: cbrower@twu.edu

Key words: aggregation / amyotrophic lateral sclerosis (ALS) (Lou Gehrig disease) / frontal temporal lobar degeneration (FTLD) / proteasome / TAR DNA-binding protein 43 (TDP-43) (TARDBP) / pre-mRNA splicing / Stathmin-2

Author Contributions: All authors have full access to the data in this study and take responsibility for the integrity of the data and accuracy of analysis. Study design and concept: W.M.M., Y.A.T.K, E.N., and C.S.B. Data acquisition: W.M.M., K.B, Y.A.T.K., K.C., S.P., E.H.,and C.S.B. Analysis and interpretation: W.M.M., Y.A.T.K, E.N., and C.S.B Drafting manuscript: W.M.M., E.N., and C.S.B.

Abbreviations

ALS: Amyotrophic lateral sclerosis;

ATE1: Arginyl-tRNA transferase 1;

AUC: Area under the curve;

BAG6: BCL2-associated athanogene 6;

CE: Cryptic exon;

CTF: C-terminal fragment;

DAVID: Database for Annotation, Visualization and Integrated Discovery;

EF1α: Elongation factor 1 alpha promoter;

FDR: False discovery rate;

FTD: Frontotemporal dementia;

FTLD: Frontotemporal lobar degeneration;

GO: Gene Ontology;

LC-MS/MS: Liquid chromatography–tandem mass spectrometry;

N-degron: N-terminal degron;

PARP: Poly(ADP-ribose) polymerase;

PQC: Protein quality control;

RRM: RNA recognition motif;

SINQ: Spectral index quantitation;

STMN2: Stathmin-2;

TARDBP: TAR DNA-binding protein gene;

TDP43 (TDP-43): TAR DNA-binding protein 43;

UNC13A: Unc-13 homolog A;

UPS: Ubiquitin–proteasome system;

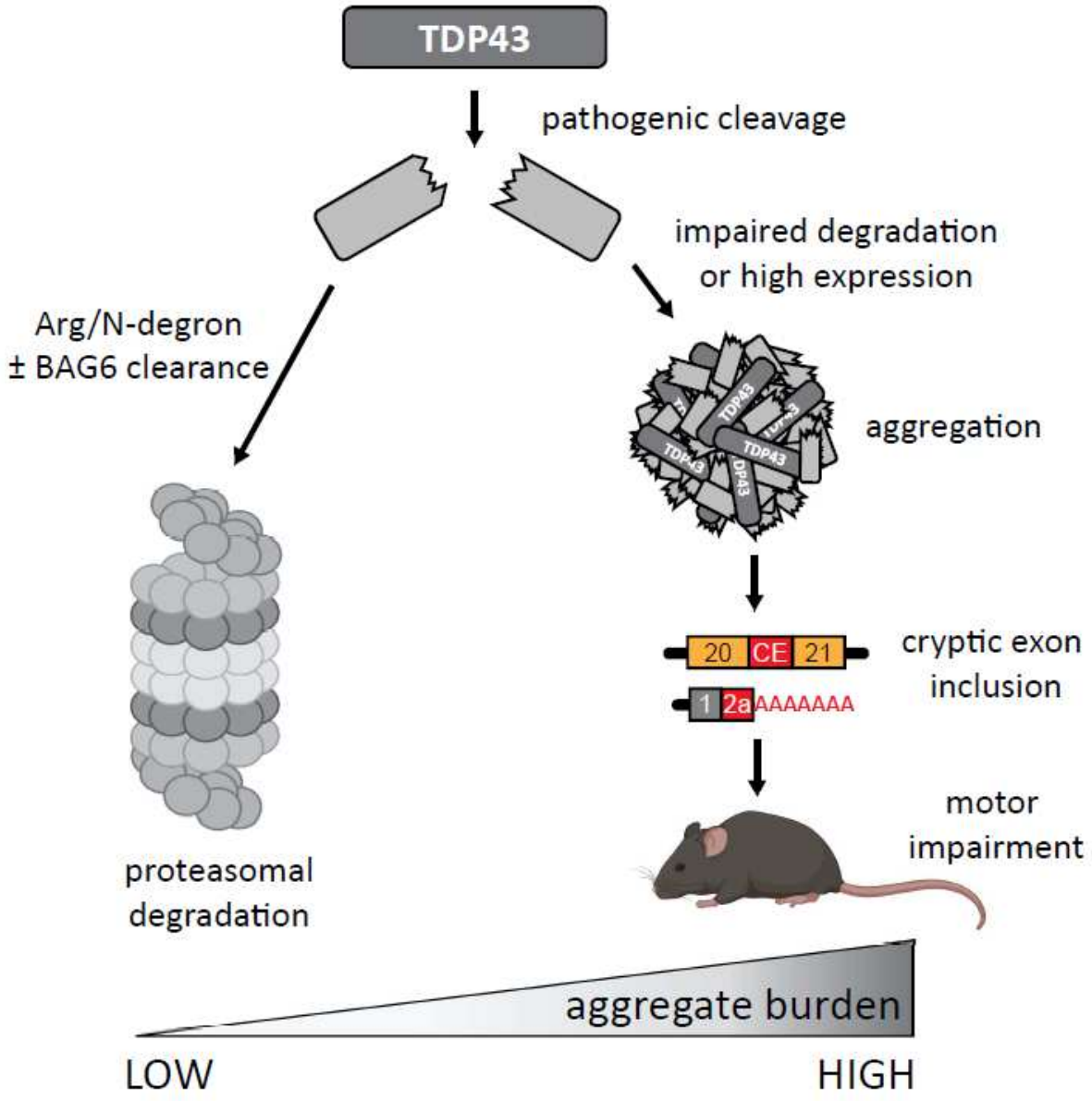
URT: Ubiquitin reference technique;

WT: Wild type.

Abstract

C-terminal fragments (CTFs) of TDP43 accumulate in neurodegenerative disease, but whether pathology arises from loss of normal TDP43 function or from toxic gain-of-function effects of the fragments remain unresolved. To address this, we examined two disease-associated fragments, $TDP43^{219}$ and $TDP43^{247}$, in cultured neurons and *in vivo* in the presence of intact endogenous TDP43, thereby isolating fragment-specific effects. $TDP43^{247}$ formed prominent cytoplasmic inclusions in neurons, whereas $TDP43^{219}$ remained largely soluble, reflecting differences in their susceptibility to protein quality control pathways. Proteomic profiling revealed that proteins detected in soluble CTF fractions were enriched for RNA splicing and post-transcriptional regulatory processes, whereas proteins detected in insoluble CTF fractions were enriched for translation-associated and metabolic pathways. Notably, accumulation of aggregation-prone $TDP43^{247}$ disrupted pre-mRNA splicing of *STMN2* and *UNC13A*, inducing cryptic exon inclusion and resulting in loss of Stathmin-2 protein. *In vivo* expression of $TDP43^{247}$ in the mouse motor cortex induced motor impairments despite the continued presence of endogenous TDP43. Together, these findings demonstrate that an elevated aggregate load of TDP43 CTFs can drive neuronal dysfunction through a toxic gain-of-function mechanism, linking impaired clearance to RNA-processing defects in the presence of intact full-length TDP43.

Graphical Abstract



Significance statement

A longstanding challenge in ALS and FTD research is determining whether TDP43 pathology arises primarily from loss of its essential nuclear functions or from toxic gain-of-function effects associated with disease-linked fragments. Proteolytic cleavage of TDP43

generates C-terminal fragments (CTFs) that are prominent constituents of pathological inclusions, yet their intrinsic contribution to disease remains unclear, in part because they are efficiently eliminated by protein quality control pathways in most experimental systems. Here, we leverage fragment-specific differences in proteostasis to isolate the effects of stabilized TDP43 C-terminal fragments in the presence of intact, endogenous TDP43. This approach reveals how selective failure of protein quality control, rather than fragment generation alone, may drive aggregation, disrupt RNA processing, and promote neuronal vulnerability. By distinguishing fragment-specific toxicity from secondary consequences of TDP43 loss-of-function, this work provides a framework linking proteolytic cleavage, impaired clearance, and selective neurodegeneration in TDP43 proteinopathies and highlights protein quality control pathways as critical modifiers of disease risk.

Introduction

Neurodegenerative diseases such as amyotrophic lateral sclerosis (ALS) and frontotemporal dementia (FTD) are characterized by the accumulation of misfolded proteins in neurons and glia [1-9]. A central unresolved question is whether pathology arises primarily from loss of essential protein functions or from toxic gain-of-function effects associated with pathological protein fragments and aggregation. The RNA-binding protein TDP43 lies at the center of this debate. Under physiological conditions, TDP43 is predominantly nuclear and regulates pre-mRNA splicing, RNA stability, nucleocytoplasmic transport, and translation, including through its participation in stress granule dynamics [10-22]. Through its glycine-rich, prion-like C-terminus, TDP43 also engages in extensive interactions with other RNA-binding proteins.

In ALS and FTD, TDP43 can mislocalize to the cytoplasm and undergo proteolytic cleavage predominantly within its second RNA recognition motif (RRM2) leading to accumulation in detergent-insoluble inclusions [6, 23-28]. Prominent components of these inclusions are CTFs enriched in low-complexity, aggregation-prone sequences that promote self-association. Whether disease arises from loss of full-length TDP43 function following cleavage or from a toxic gain-of-function mediated by the resulting aggregation-prone fragments remains unresolved. In particular, it is unclear whether CTF accumulation disrupts RNA-processing networks in the presence of intact endogenous TDP43, or whether RNA dysregulation strictly reflects loss of full-length TDP43 function.

Immortalized cell lines, including HEK-293 and neuroblastoma-derived models, have been instrumental in defining protein quality control (PQC) pathways responsible for TDP43 CTF clearance. In these systems, both $TDP43^{219}$ and $TDP43^{247}$ undergo ATE1-dependent arginylation and degradation via the Arg/N-degron pathway [29, 30], while $TDP43^{219}$ is additionally recognized by the BAG6 complex, which directs hydrophobic substrates toward ubiquitin-dependent proteasomal clearance [31]. Although these models are well suited for dissecting fragment-specific degradation mechanisms, their robust and partially redundant PQC capacity may limit evaluation of fragment-associated toxicity. Accordingly, defining the pathological potential of TDP43 CTFs requires paradigms in which fragment stabilization and aggregation burden can be precisely controlled and assessed in more disease-relevant cellular contexts.

Disentangling toxic gain-of-function effects from the consequences of TDP43 loss-of-function requires systems in which pathological fragments are examined in the presence of intact, endogenous TDP43. This distinction is critical because loss of TDP43 function is known

to cause widespread RNA-processing defects, including cryptic exon inclusion in transcripts such as *STMN2* and *UNC13A*, which contribute to axonal dysfunction and synaptic impairment [32-35]. Whether stabilized, aggregation-prone CTFs can disrupt these endogenous RNA programs without overt depletion of full-length TDP43 remains an essential unanswered question.

Here, we address this issue by focusing on two closely related, disease-associated TDP43 C-terminal fragments, TDP43^{219} and TDP43^{247}, which are major components of pathological aggregates in ALS and FTD [2-9]. Although largely identical in sequence, these fragments differ in their susceptibility to distinct PQC pathways [30], providing a unique opportunity to dissect how fragment-specific degradation mechanisms influence aggregation, protein interactions, and neuronal vulnerability. We examined these fragments in primary neuronal cultures, *in vivo* in mice, and in human cell models including SH-SY5Y cells, while preserving endogenous full-length TDP43. Through this integrated approach, we sought to determine whether stabilization of aggregation-prone CTFs is sufficient to drive disease-relevant neuronal dysfunction and to define how aggregation burden alters TDP43-centered RNA-processing networks.

Materials and Methods

Miscellaneous reagents: MG132 (10012628; Caymen Chemical). Anti-C-terminal TDP43 (12892-1-AP; Proteintech), anti-FLAG M2 (F1804; Sigma Aldrich), and anti-PARP (9542; Cell Signaling Technology). Secondary antibodies: anti-mouse IgG (H + L)-AlexaFluor488 (A-11001), anti-rabbit IgG (H + L)-AlexaFluor488 (A-11034), anti-mouse IgG DyLight 680 (35519), anti-mouse IgG DyLight 800 (SA5- 10176), anti-rabbit IgG DyLight 680 (35569), and

anti-rabbit IgG DyLight 800 (SA5-10036) were from Thermo Fisher Scientific. DAPI (4',6-diamidino-2-phenylindole; F6057; Sigma Aldrich)

Plasmids: To generate AAV-based plasmids expressing Val-TDP43^{247} driven by the EF-1α promoter (pCB559), DNA encoding mCherry-Ub^{K48R}-Val^{247}-TDP43^{f} was amplified from pCB401 using primers CB523F and CB524R and used to replace the Cre cDNA in pAAV-Ef1α-Cre after digestion with KpnI/EcoR1. (pAAV-EF1α-Cre was a gift from Karl Deisseroth; Addgene # 55636) [36]. To generate lentiviral-based expression plasmids expressing mCherry-Ub^{K48R}-Val^{219}-TDP43^{f} (pYK053) and mCherry-Ub^{K48R}-Val^{247}-TDP43^{f} (pYK054) driven by the CMV promoter, pCB557 and pCB559 were digested with BamHI/EcoRV and cDNA inserts were ligated into BamHI/EcoRV-cut pLenti CMV GFP Hygro (656-4) (Addgene #17446). For the control plasmid expressing mCherry-Ub^{K48R} only (pYK052), we used the Q5 site directed mutagenesis kit according to the manufacturer's protocol. Briefly, we used YK54F and YK55R to insert a stop codon after the coding sequence of ubiquitin in pYK053. PCR was carried out for 25 cycles, and 1 µl of the resulting reaction mix was then used in a kinase-ligase-DpnI (KLD) reaction for 5 min at room temperature (RT) to obtain ligation and template removal. NEB stable 10 cells (New England BioLabs) were transformed with 5 µl of the KLD reaction mixture and selected on LB plates supplemented with ampicillin (100 µg/ml). To enhance post-transcriptional stability of the transcript in transduced cells, the Woodchuck Hepatitis Virus Posttranscriptional Regulatory Element (WPRE) was amplified from pLenti-CMV-GFP-Hygro using primers YK58F and YK59R. The resulting amplicon was digested with EcoRV and XhoI and ligated into pYK052, pYK053, and pYK054 downstream of the cDNAs at the EcoRV/XhoI sites to generate pYK056 (expressing mCherry-Ub^{K48R}), pYK057 (expressing mCherry-Ub^{K48R}-Val^{219}-TDP43^{f}),

and pYK058 (expressing mCherry-Ub^{K48R}-Val^{247}-TDP43^{f}) respectively. Lentiviruses was packaged by Applied Biological Materials Inc (Canada).

Cell culture, transfection, and electroporation: Human neuroblastoma SH-SY5Y and human embryonic kidney (HEK-293T) cells were maintained at 37°C with 5% CO_2 in Dulbecco's Modified Eagle Medium (DMEM; Corning Cellgro). For SH-SY5Y cells, DMEM/F12 was used, whereas HEK-293T cells were maintained in DMEM. Media were supplemented with 10% fetal bovine serum (Gemini Bio-Products), 20 mM glutamine, 100 U/mL penicillin, and 0.1 mg/mL streptomycin (Fisher Bioreagents). HEK-293T cells were transfected using the BioT transfection reagent (Bioland Scientific) according to the manufacturer's instructions. SH-SY5Y cells at ~60-70% confluency were trypsinized and resuspended in OPTI-MEM lacking antibiotics and fetal bovine serum. Cells were transferred to 0.4-cm gap Gene Pulser electroporation cuvettes (Bio-Rad) and electroporated at 0.19 kV with a capacitance of 0.950 μF using a Gene Pulser II electroporation system (Bio-Rad). Cells were plated immediately following electroporation, and culture medium was replaced the following day to remove dead cells.

Primary neuronal cultures: Post-natal day 1 (P1) mouse pups from wild type C57BL/6 mice were dipped in 70% alcohol and the heads separated from the body with sterilized blades. The skull was cut from the base to the nose using sterile scissors and a pair of forceps. The forceps were used to gently separate the skin and skull while scooping out the brain from the cavity. Scooped brains were placed in sterile phosphate buffered saline (PBS). The brains were then minced with sterile blades and transferred into tubes with medium A (neurobasal plus medium, B27 plus supplement, glutamax and penicillin/streptomycin cocktail (ThermoFisher). The tubes

were placed at 32°C to shake at 300 rpm for 5 mins. The medium in the tube was then discarded and medium B (containing Neurobasal plus medium, papain 2mg/ml, and penicillin/streptomycin cocktail) was added to the tube. Minced samples were then incubated at 33°C, 300 rpm, for 30 mins. Once completed, the media in the tube was discarded and medium A was added and the samples were incubated at RT for 5 mins. The samples were triturated with a polished Pastier pipette ten times and supernatant was moved to a fresh clean tube. The samples were centrifuged at 200xg for 5 mins and the pellet resuspended in medium C (consisting of neurobasal plus medium, B27 plus supplement, and glutamax). Cells were counted and plated in poly-D-lysine coated plates. A media change was performed 6 h post plating. The cells were infected with lentivirus expressing mCherry alone, mCherry-Val-TDP43^{219} or mCherry-Val-TDP43^{247} with an MIO of <1.0 to ensure non-infected control cells exist in the same culture. Transduction efficiency was verified by mCherry fluorescence five days post-infection. CTF expression and aggregation was detected immunocytochemically using a mouse anti-FLAG primary antibody and an Alexa488 secondary antibody.

Immunocytochemistry: To examine fragment expression in primary neuronal culture, cells grown on coverslips were washed three times with PBS for 5 mins each wash. Fixed with freshly made 4% paraformaldehyde for 15 mins at RT. The coverslips were washed once with PBS. Permeabilized with 0.5% Triton X-100 for 15 mins at RT. The coverslips were washed three times with PBS for 5 mins each wash. Blocked for 1 h using 10% goat serum made with PBS. An anti-FLAG primary antibody was used to incubate for 3 h at 37°C or overnight at 4°C. Followed by washing three times with PBS containing 0.1% Tween 20. An anti-mouse AlexaFluor488 secondary antibody was used to incubate for 1 h at 37°C. Post incubation, the

samples were washed three times with PBS containing 0.1% Tween 20 for 5 mins each wash. One final was performed with PBS. Once all solutions were decanted, DAPI counterstain was added to microscopic slides and mounted coverslips for imaging using the Zeiss LSM 900 confocal microscope.

Immunoblotting: To validate expression of mCherry, TDP43 C-terminal fragments and endogenous TDP43, HEK-293T cells and primary neuronal culture were infected with lentiviral vectors expressing mCherry-ub (control), mCherry-TDP43^{219} and mCherry TDP43^{247} fragments and checked for expression of C-terminal fragments and mCherry-Ub. To determine whether TDP43 fragments induce toxicity in cells, levels of caspase 3 and poly-[ADP-ribose] polymerase 1 (PARP1) were examined. After 48 hours of infection in HEK-293T cells and 5 days of transduction in primary neurons, cells were harvested and lysed in tissue lysis buffer (TLB; 50 mM HEPES, 10% glycerol, 0.05% NP-40, 150 mM NaCl, 1mM DTT and 1 mM PMSF containing the complete protease-inhibitor mixture) by freezing/thawing. The lysate was then centrifuged at 13,000 rpm for 20 mins at 4°C and the supernatant was collected as the soluble fraction. The pellet was washed twice in TLB, resuspended in 8M urea buffer (8 M urea, 50 mM Tris, 1 mM DTT and 1 mM PMSF), sonicated and centrifuged at 13,000 rpm for 10 mins at RT. The final supernatant was collected as the "insoluble" fraction. Protein concentration for both soluble and insoluble fractions was determined using the BioRad Protein Assay reagent (BioRad) according to manufacturer's protocol. Prior to SDS-PAGE, samples were normalized, boiled at 95°C for 10 mins to denature proteins. Normalized protein samples were separated on a 4 -12% gradient NuPage Bis-Tris premade gels (Invitrogen) and transferred onto methanol activated PVDF membrane (BioRad), in Towbin buffer (25 mM Tris, 192 mM glycine and 20% methanol)

overnight at 4°C. Membranes were blocked in 5% milk made with nonfat dry milk in PBS plus 0.1% Tween 20 at RT for 1 hour. Membranes were then incubated in primary antibodies; anti-Caspase 3 (9662, Cell signaling), Anti-PARP1 (C-2-10; BML-SA250; Enzo), anti-FLAG M2 (F1804, Sigma Aldrich), anti-TDP43 C-terminal fragment (12892-1-AP, Proteintech); (1:1000 dilution in 5% milk in PBS containing 0.1% Tween 20 for all primary antibodies) overnight at 4°C or for 3 h at RT. The membranes were washed three times for 5 min with PBS plus 0.1% Tween20 for 5 min, incubated with secondary antibodies (1:7000 dilution) as indicated for 1 h at RT. Thereafter, blots were washed three times with PBS plus 0.1% Tween 20, twice in PBS, and imaged using the Licor Odyssey CLx system.

Reverse Transcriptase-Polymerase Chain Reaction (RT-PCR): Total RNA was isolated from HEK-293T and SH-SY5Y cells 72 h post-transfection/electroporation using the Thermo Scientific GeneJET RNA Purification Kit (catalog #K0731) according to the manufacturer's instructions. Genomic DNA was removed by incubating 2 µg of RNA with DNase I in the presence of 10× NEB Buffer 2, 50 mM $MgCl_2$, and nuclease-free water at 37°C for 30 min. DNase activity was inactivated by addition of 2 µl of 50 mM EDTA followed by incubation at 75°C for 10 min. For cDNA synthesis, DNase-treated RNA was mixed with oligo(dT) primers, denatured at 65°C for 5 min, briefly centrifuged, and placed on ice. Reverse transcription reactions were prepared using ProtoScript II Reverse Transcriptase (New England Biolabs; E6560), with ProtoScript II Enzyme included in +RT reactions or replaced with nuclease-free water for -RT controls. Reactions were incubated at 42°C for 1 h, followed by enzyme inactivation at 80°C for 5 min. PCR amplification was performed using gene-specific primers to detect cryptic and correctly spliced transcripts. *STMN2* cryptic exon 2a inclusion was amplified

using primers WM001F and WM002R (205 bp), while normally spliced *STMN2* transcripts (exon 1 - exon 2 junction) were amplified using primers WM003F and WM004R (142 bp). *UNC13A* cryptic exon inclusion (exon 21 junction) was amplified using primers WM007F and WM008R (281 bp), and correctly spliced UNC13A transcripts (exon 20 - exon 21 junction) were amplified using primers WM005F and WM006R (189 bp). PCR products were resolved on 2% agarose gels containing ethidium bromide and visualized using a Bio-Rad ChemiDoc imaging system. Amplicons containing cryptic exons were excised, gel-purified, and verified by Sanger sequencing using primers WM001F/WM002R (*STMN2*) and WM007F/WM008R (*UNC13A*).

Animals: All animal procedures were approved by the Texas Woman's University Institutional Animal Care and Use Committee and were conducted in accordance with institutional and federal guidelines. A total of 36 wild-type mice were used in this study. Mice were of C57BL/6 origin or a mixed C57BL/6 × DBA/2 background and included equal numbers of males and females (18 per sex). Animals were randomly assigned to one of three experimental groups (n = 12 per group) for stereotaxic injection with lentivirus expressing either mCherry-Ub alone, mCherry-Ub-TDP43^{219}, or mCherry-Ub-TDP43^{247}. Mice were housed in ventilated cages with *ad libitum* access to food and tap water. Mice were maintained on a 12 h light/dark cycle at ambient temperature of 23 ± 3°C and humidity of 50 ± 20%. Light-dark cycle, humidity controlled

Mice stereotaxic surgery and Lentiviral Injection: Wild type mice with an average age of 135 days were anesthetized with the isoflurane 2-3% induction and 1-2% maintenance rate throughout surgery. Mice were secured in a stereotaxic frame (Kopf Instruments) Ophthalmic

ointment was applied bilaterally to prevent corneal drying. A midline incision exposed the skull and bupivacaine hydrochloride (0.25%, 50 µL) was applied topically for local analgesia. The skull was leveled along sagittal and coronal planes. Coordinates for the motor cortex were set relative to bregma: anterior/posterior (Y: +1.55 mm), medial/lateral (X: +1.2 mm), dorsal/ventral (Z: -1.00 mm). Approximately 5 µL of viral vectors were unilaterally injected at a rate of 0.2 µL/min using a Hamilton syringe. The syringe was left in place for 5 mins post-injection to prevent backflow, then slowly withdrawn. The incision was closed with absorbable sutures, and neomycin sulfate ointment was applied to minimize infection risk. Surgeries were performed using standard aseptic techniques per AVMA guidelines.

Beam walking: Eight months post-surgery, mice were assessed using the balance beam test. Animals were placed on a brightly lit elevated platform with beams of varying widths (6 mm, 10 mm, and 15 mm) and allowed to traverse the beam toward a dark goal box containing bedding and food to encourage movement. Each mouse completed three trials per beam. Outcome measures included the average time to traverse the beam, the average number of foot slips, and the total distance traveled, averaged across trials.

Gait Analysis: The footprint/gait tunnel test was performed using a constructed tunnel containing white watercolor sheets of paper leading to a black box. Mice forelimbs and hindlimbs were painted with non-toxic washable ink (blue for forelimbs and black for hindlimbs). Room acclimated mice were placed at the brightly lit tunnel entrance to walk into the black box containing food and bedding. After each run, mice paws were wiped clean, a clean sheet of paper was used for each mouse, and the apparatus was cleaned with 70% ethanol between animals.

Dried footprint papers were scored blinded using sequences of >4 consecutive clear steps per limb (excluding the first and last prints). Three trials were run for all mice. The metrics measured in centimeters were: *stride length* (center to center distance between consecutive prints of the same paw), *stride width* (perpendicular distance between left and right paw centers), and *toe spread* (distance between tips of digits 1 and 5). The metrics were quantified for forelimbs and hindlimbs, averaged per limb per animal over three trials. Non-scorable trials were repeated after >10 mins rest with a maximum of three attempts per session.

Rotarod: Motor coordination and balance were assessed using an accelerating rotarod apparatus. Mice were acclimated to the behavioral testing room for 1 h prior to testing. During each trial, mice were placed on a rotating rod that accelerated from 4 to 40 rpm over a 5-min period (300 s). A trial ended when the mouse fell from the rod. If a mouse fell or clung to the rod for one full rotation within the first 5 s, the trial was terminated and repeated. Each mouse underwent three trials per time point, and performance values were averaged for analysis. Latency to fall and rotational speed at the time of fall were recorded. The rotarod apparatus was cleaned with 70% ethanol between animals. Behavioral testing was conducted monthly beginning 1 month post-surgery and continued until study termination at 10 months post-surgery.

Hindlimb clasp: The hindlimb clasping test was scored as before [37, 38]. Briefly, mice were acclimated to the procedure room for at least 1 h before testing, then gently grasped at the base of the tail and lifted so that the body was fully suspended. Hindlimb position was observed for 10 seconds and scored by an observer blind to treatment. Scoring was as follows: hindlimb consistently splayed away from abdomen = 0; one hindlimb retracted toward the abdomen for

more than 50% of the suspension = 1; both hindlimbs partially retracted toward the abdomen for more than 50% of the suspension = 2; both hindlimbs fully retracted and touching the abdomen for more than 50% of the suspension = 3. Following scoring, the mice were returned to their home cages.

Transcardiac perfusion and brain dissection: Mice were deeply anesthetized by isoflurane inhalation in a chemical fume hood. Isoflurane was applied to a cotton ball placed inside a 50-mL conical tube, and mice were inserted nose-first into the tube and gently manually restrained until deep anesthesia was achieved. Following anesthesia, mice were transcranially perfused under a fume hood with PBS, followed by fixation with freshly prepared 4% paraformaldehyde (PFA). Animals were positioned supine, the thoracic cavity was opened, and the heart was exposed. A blunt perfusion needle was inserted into the left ventricle, and the right atrium was incised to allow outflow. PBS was perfused at a constant rate until the effluent was clear of blood, followed by 4% PFA. Brains were dissected and post-fixed overnight in 4% PFA, then transferred to 30% sucrose for cryoprotection. Tissue was frozen and sectioned coronally at 30 µm using a Leica SM2000 sliding microtome.

Immunohistochemistry: To validate injection site, fixed brain sections were washed three times with 1X PBS for 5 mins each to remove residual fixative. Non-specific binding was blocked by incubating tissues with 10% goat serum in PBS for 1 h at 37°C and then incubated with anti-glial fibrillary acidic protein (GFAP) antibody (1:500 dilution in PBS) for 2 h at 37°C to detect necrotic tissue. Tissues were washed three times with PBS containing 0.1% Tween 20 for 5 mins each and then incubated with an anti-mouse Alexa Fluor 488-conjugated secondary antibody

(1:1000 dilution in PBS) for 1 h at 37°C. Tissue was washed again three times with PBS containing 0.1% Tween 20 for 5 mins each, followed by a final wash with PBS. Sections were mounted using Fluoroshield with DAPI (Sigma) and imaged using a Zeiss LSM confocal microscope.

Mass spectrometry: HEK-293T cells were transfected with plasmids expressing DHFR-Ub^{K48R} (pYK027), or $TDP43^{219}$ (pCB328) and $TDP43^{247}$ (pCB332) bearing N-terminal Val from the P_{CMV} promoter and treated with 5 μM MG132 for 24 h. Forty-eight h post-transfection, soluble and insoluble lysates were made as described above and proteins were immunoprecipitated using anti-FLAG magnetic beads as described above. Eluted proteins were run 1cm into 4-12% gradient NuPage Bis-Tris gel (Invitrogen), stained with coomassie, minced, and submitted to the UT Southwestern Proteomics core where protein gel pieces were digested overnight with trypsin (Pierce) following reduction and alkylation with DTT and iodoacetamide (Sigma-Aldrich). The samples then underwent solid-phase extraction cleanup with Oasis HLB plates (Waters) and the resulting samples were analyzed by LC/MS/MS using an Orbitrap Elite mass spectrometer (Thermo Electron) coupled to an Ultimate 3000 RSLC-Nano liquid chromatography systems (Dionex). Samples were injected onto a 75 μm i.d., 15-cm long EasySpray column (Thermo), and eluted with a gradient from 1-28% buffer B over 60 min. Buffer A contained 2% (v/v) ACN and 0.1% formic acid in water, and buffer B contained 80% (v/v) ACN, 10% (v/v) trifluoroethanol, and 0.1% formic acid in water. The mass spectrometer operated in positive ion mode with a source voltage of 2.8 kV and an ion transfer tube temperature of 275°C. MS scans were acquired at 240,000 resolution in the Orbitrap and up to 14 MS/MS spectra were obtained in the ion trap for each full spectrum acquired using collisionally-induced dissociation (CID),

with charge 1 ions rejected. Dynamic exclusion was set for 15 s after an ion was selected for fragmentation.

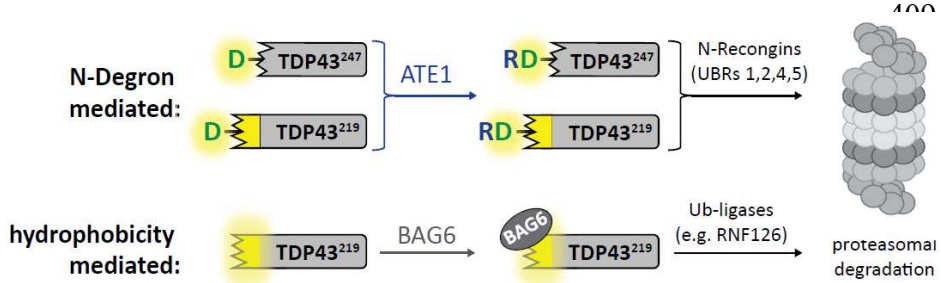
Peptide Identification: Raw MS data files were converted to a peak list format and analyzed using the Central Proteomics Facilities Pipeline (CPFP), version 2.0.3 [39, 40]. Peptide identification was performed using the X!Tandem [41] and open MS search algorithm (OMSSA) [42] search engines against the appropriate protein database from Uniprot, with common contaminants and reversed decoy sequences appended [43]. Fragment and precursor tolerances of 20 ppm and 0.6 Da were specified, and three missed cleavages were allowed. Carbamidomethylation of Cys was set as a fixed modification and oxidation of Met was set as a variable modification. Label-free quantitation of proteins across samples was performed using SINQ normalized spectral index Software [44].

Gene Ontology (GO) analysis: Gene Ontology (GO) enrichment analysis of biological processes was performed on proteins selectively enriched with soluble or insoluble TDP43 CTFs. Specifically, 38 proteins enriched with soluble CTFs and 68 proteins enriched with insoluble CTFs that were not also associated with DHFR-Ub were analyzed using the Database for Annotation, Visualization and Integrated Discovery (DAVID) [45]. Functional annotation was conducted using GO terms corresponding to biological process (GOTERM_BP_DIRECT). GO terms with significant enrichment, defined as a false discovery rate (FDR) ≤ 0.05, are reported. For each significantly enriched term, fold enrichment values were calculated and plotted.

Results

Metabolism of proteolytic C-terminal fragments of TDP43

We previously reported that the intracellular aggregation of disease-associated CTFs of TDP43 is prevented by multiple UPS-mediated quality-control pathways. Two such fragments, TDP43^{219} and TDP43^{247}, major components of pathological aggregates in ALS/FTD patient tissue, bear N-terminal Asp- upon cleavage and undergo rapid N-degron-mediated proteasomal degradation. This process requires their N-terminal arginylation by Arginyl-tRNA transferase 1 (ATE1), followed by poly-ubiquitylation by N-Recognin E3 ligases and subsequent proteasomal degradation [29, 30]. In the absence of ATE1, TDP43^{247} accumulates and forms insoluble inclusions closely resembling those observed in vulnerable neuronal populations in ALS and FTD models [8, 30, 46]. In contrast, TDP43^{219} continues to be degraded due to extended hydrophobicity recognized by the BAG6 complex, which recruits E3 ligases such as RNF126 to direct its ubiquitylation and clearance (Fig. 1) [31]. As a result of this additional PQC pathway, TDP43^{219} aggregates are rare, whereas TDP43^{247} aggregates accumulate robustly in ATE1-deficient cells [30].



Aggregation Dynamics of TDP43^{219} and TDP43^{247} in Neurons

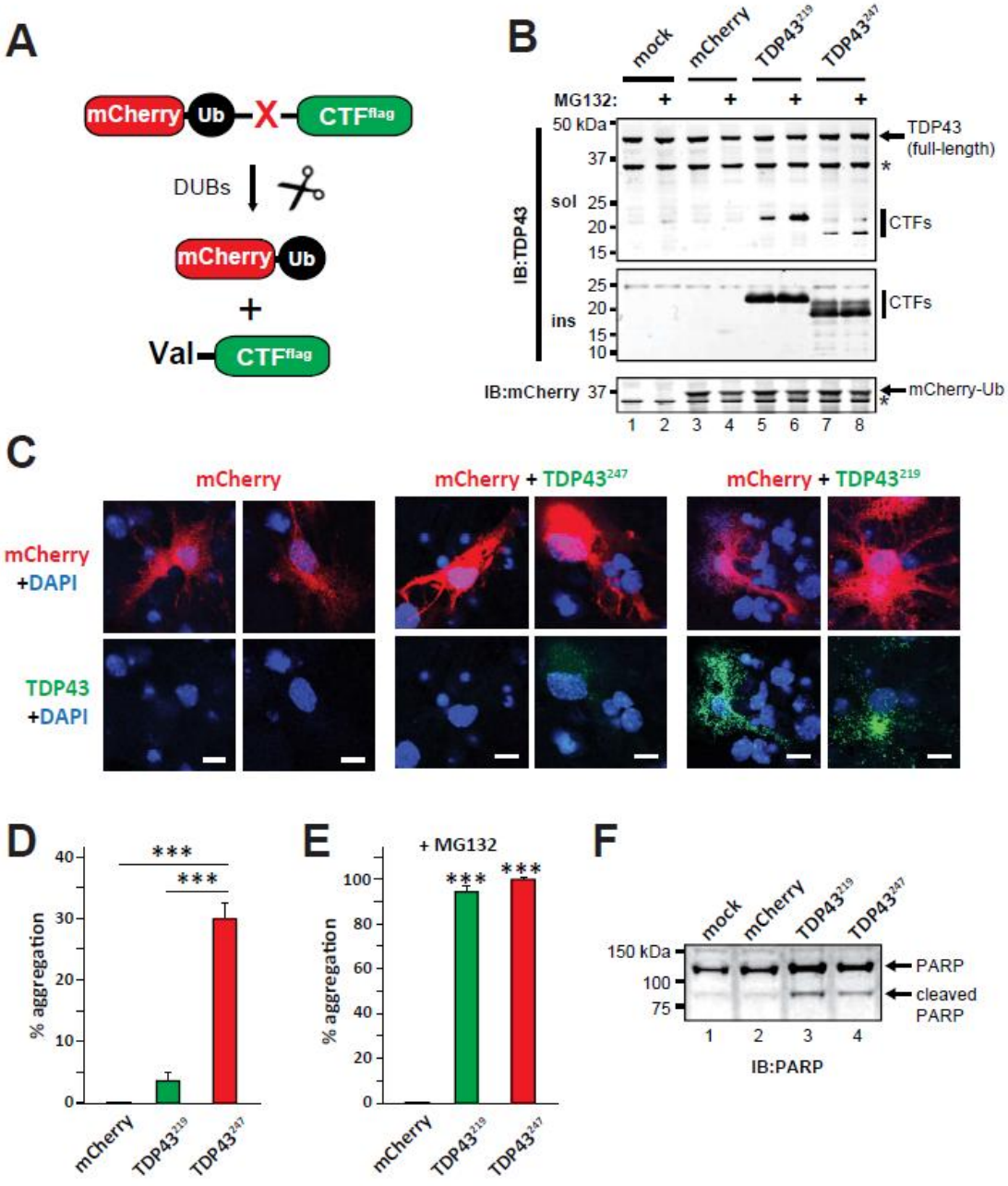
To demonstrate neuronal aggregation propensities of TDP43^{219} and TDP43^{247}, we used lentiviral delivery of URT-based constructs to express mCherry-Ub, mCherry-Ub-TDP43^{219}, and

417 mCherry-Ub-TDP43^{247} (Fig 2A). Co-translational cleavage of the mCherry-Ub fusion generates
418 a stable mCherry-Ub^{R48} that marks transduced cells, as well as a C-terminally FLAG-tagged CTF
419 whose fate can be visualized by indirect immunofluorescence using an anti-FLAG antibody with
420 a fluorescein-conjugated secondary. The URT also enables expression of CTFs bearing N-
421 terminal Val, allowing them to escape from ATE1-dependent Arg/N-degron-mediated
422 degradation. To validate expression and to determine how each CTF partitions between
423 detergent-soluble and -insoluble fractions, we infected HEK-293T cells and performed
424 immunoblotting with a C-terminal TDP43 antibody three days post-infection. Whereas TDP43^{219}
425 was detected in both soluble and insoluble fractions, TDP43^{247} was predominantly recovered in
426 the insoluble fraction (Fig 2B).

427 Expression of Val-TDP43^{247} in cultured neurons produced prominent perinuclear
428 aggregates in ~30% of mCherry-positive (infected) cells (Fig 2C and D), whereas only ~4% of
429 neurons expressing TDP43^{219} displayed aggregates (Fig 2C and 2D). Moreover, Val-TDP43^{247}
430 formed noticeably larger inclusions, in contrast to the small and sparse aggregates of Val-
431 TDP43^{219} (Fig 2C). Consistent with our prior work in Neuro2a cells, TDP43^{247} is predominantly
432 cleared by the ATE1-dependent N-degron pathway, whereas TDP43^{219} is additionally subject to
433 BAG6-mediated quality control [30, 31]. Proteasome inhibition with MG132 caused robust
434 aggregation of both Val-TDP43^{219} and Val-TDP43^{247} in 95% and 100% of cells, respectively
435 (Fig. 2E), indicating that the UPS plays a critical role in preventing TDP43 CTF aggregation in
436 neurons.

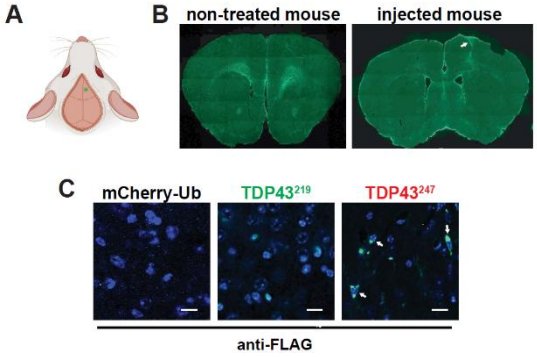
437 Poly(ADP-ribose) polymerase (PARP) is a well-established substrate of activated
438 caspases, particularly caspase-3, and its cleavage is a hallmark of apoptosis. [47]. To determine
439 whether expression of TDP43 CTFs induces apoptosis in neurons, we assessed PARP cleavage

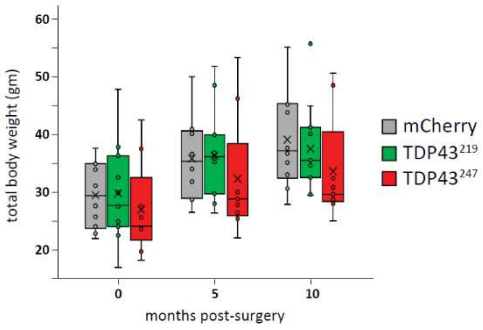
following lentiviral expression of mCherry, Val-TDP43^{219}, or Val-TDP43^{247}. Immunoblot analysis revealed increased levels of cleaved PARP in neurons expressing Val-TDP43^{219} or Val-TDP43^{247} compared with mock- or mCherry-infected controls. Together, these data indicate that neuronal expression of TDP43 CTFs is associated with activation of apoptotic signaling under these conditions (Fig 2F).

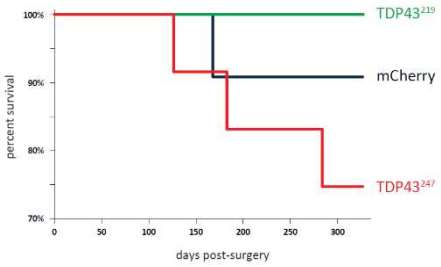


Motor Deficits and Toxicity from Stabilized TDP43 Fragments in Wild-Type Mice

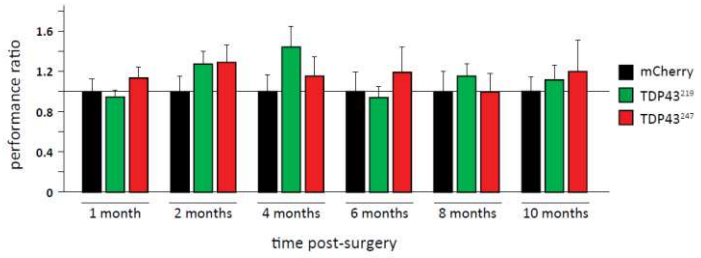
To determine whether CTFs can initiate neurodegeneration without loss of full-length TDP43, we delivered CTFs to wild-type mice (i.e., mice expressing endogenous, functional TDP43) using lentiviral vectors. We stereotaxically injected lentiviral constructs, mCherry-Ub, mCherry-Ub-Val-TDP43^{219}, or mCherry-Ub-Val-TDP43^{247} into the primary motor cortex of the right hemisphere (Fig S1A), enabling localized expression of each fragment in an otherwise TDP43-competent background, and monitored the mice for up to 10 months post-surgery. Accurate targeting of the primary motor cortex was confirmed postmortem by anti-GFAP immunostaining, which revealed sustained astrocyte activation (Fig S1B). Consistent with our findings in cultured neurons, perinuclear aggregation of TDP43^{247} was observed in a subset of cells within the motor cortex of mice injected with Val-TDP43^{247}, but not in control mice (Fig S1C). No significant differences in body weight were observed between groups throughout the experiment (Fig. S2). Approximately 25% of mice expressing Val-TDP43^{247} either died or reached a humane endpoint prior to the 10-month study duration (Fig. S3). Despite this reduced survival rate, surviving mice exhibited no significant differences in their ability to maintain or gain weight (Fig. S2).



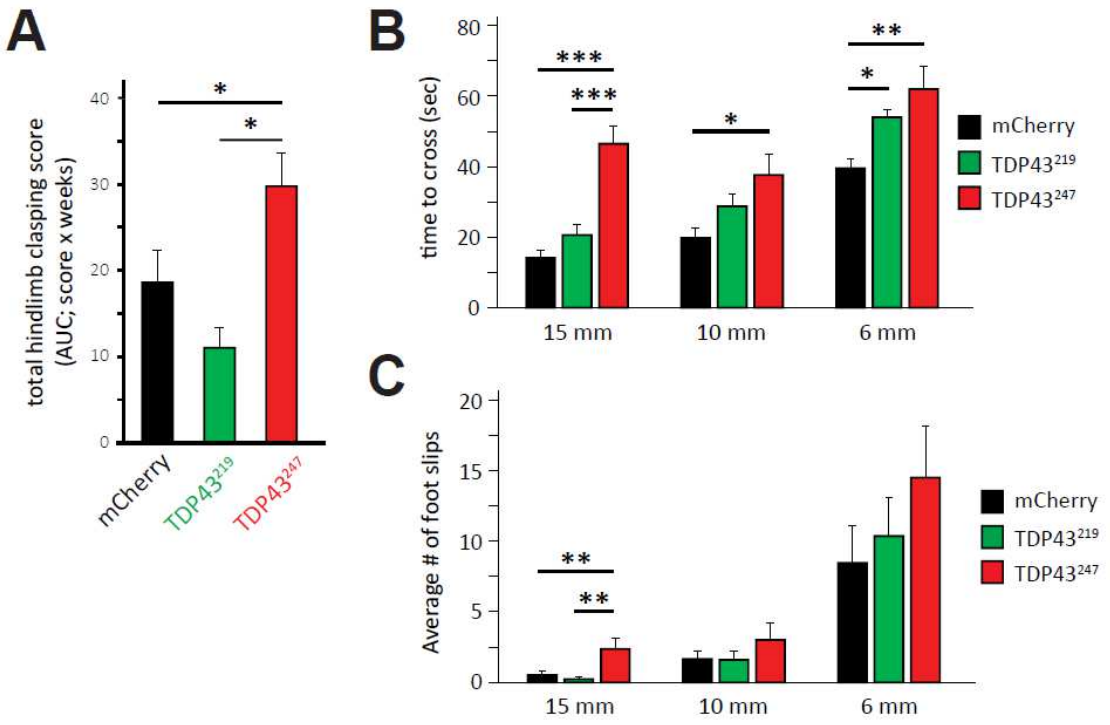




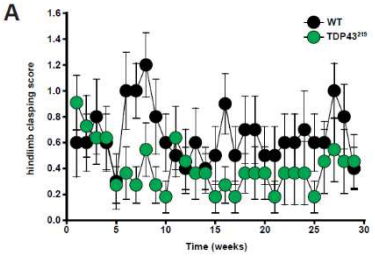
To assess motor function *in vivo*, we evaluated gross motor coordination and balance using the accelerating rotarod assay and neurological impairment using the hindlimb clasping test. Accelerating rotarod performance did not reveal significant differences in motor coordination or balance between mice expressing either TDP43 CTFs and control mice expressing mCherry-Ub alone (Fig. S4) [48].

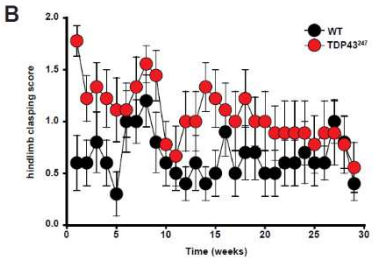


In contrast, hindlimb clasping analysis performed for up to 30 weeks post-surgery revealed a significant increase in overall clasping scores, averaged across all time points, in mice expressing $TDP43^{247}$ compared with mice expressing mCherry alone or $TDP43^{219}$ (Fig. 3A),



despite the absence of progressive worsening over time (Fig. S5). This lack of progression may reflect an early, non-propagating effect of CTF expression and aggregation in our experimental paradigm.

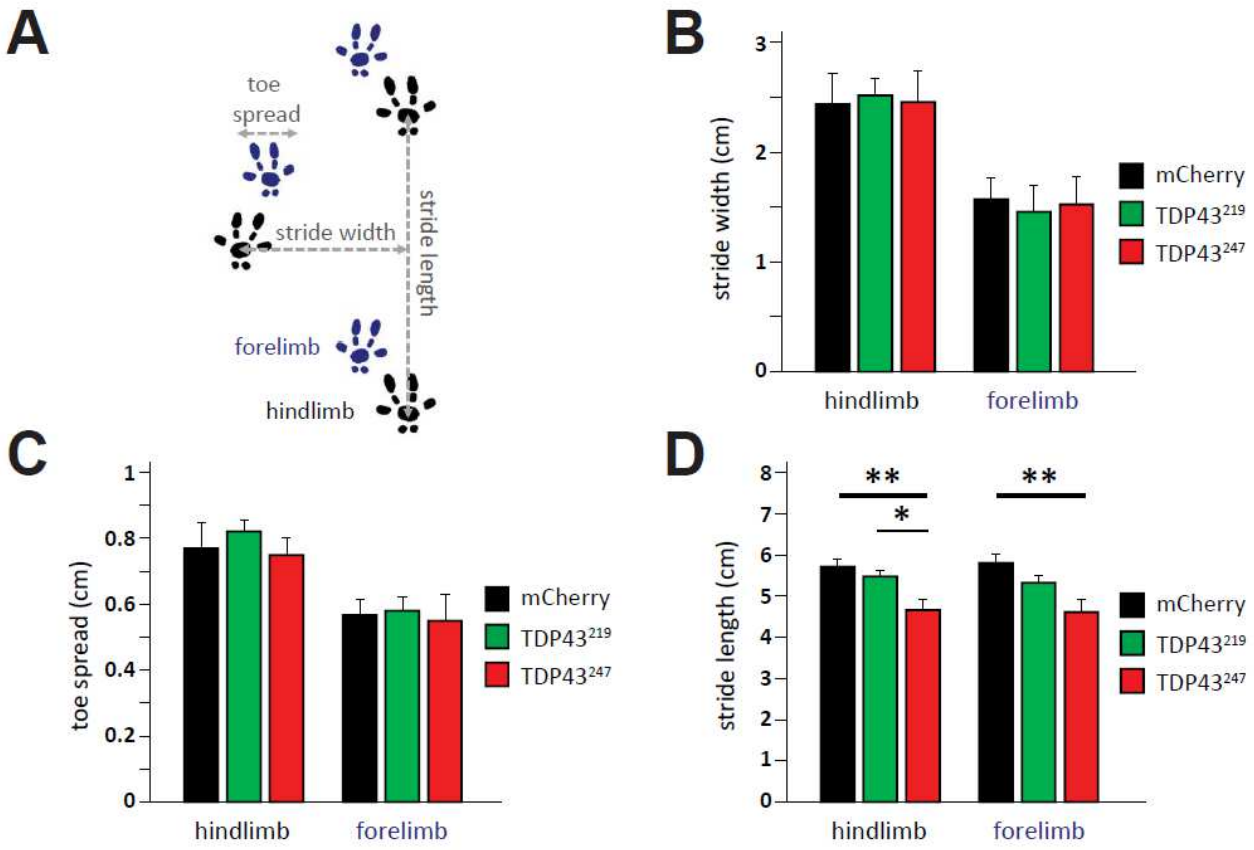




Because tasks requiring skilled motor coordination and movement precision place greater demands on motor cortex function [49, 50], we next assessed motor cortex-dependent performance using the balance beam assay [51] at 10 months post-surgery. This point coincides with detectable accumulation of $TDP43^{247}$ aggregates in the motor cortex of expressing mice. Mice were tested on beams of varying widths (6 mm, 10 mm, or 15 mm) and performance was quantified by traverse time and foot slips. Strikingly, $TDP43^{247}$ expressing mice required significantly more time to cross the beam at all widths compared to mice expressing mCherry-Ub alone or $TDP43^{219}$ (Fig 3B). Furthermore, $TDP43^{247}$ expressing mice exhibited significantly more foot slips when crossing the 15 mm beam compared to either control or $TDP43^{219}$ mice (Fig 3C).

We further analyzed gait in mice 10 months post-surgery (Fig 4A). Although stride width (Fig 4B) and toe spread (Fig 4C) were not significantly different among the groups, $TDP43^{247}$-expressing mice displayed significantly reduced forelimb and hindlimb stride length compared to mice expressing mCherry-Ub alone or $TDP43^{219}$ (Fig. 4D). Consistent with their impaired balance-beam performance, these gait alterations indicate deficits in motor cortex-dependent coordination and locomotor control. Collectively, these findings demonstrate that the accumulation of aggregation-prone TDP43 C-terminal fragments, most prominently $TDP43^{247}$

selectively impair motor cortex-dependent motor coordination and locomotor precision without broadly disrupting baseline gait parameters.



Aggregation-Dependent Interactomes of TDP43 C-Terminal Fragments Reveal Distinct Functional Enrichment.

Previous mass-spectrometry studies have shown that full-length TDP43 interacts with proteins involved in RNA splicing and translation, consistent with its established roles in RNA metabolism [52]. To determine how disease-associated CTFs alter this interactome, we performed LC-MS/MS analysis on proteins co-immunoprecipitated with Val-TDP43^{219} and Val-TDP43^{247}. Associated proteins were isolated from both the detergent-soluble fraction (Table S2) and an insoluble fraction, which was subsequently urea-solubilized and renatured (Table S3).

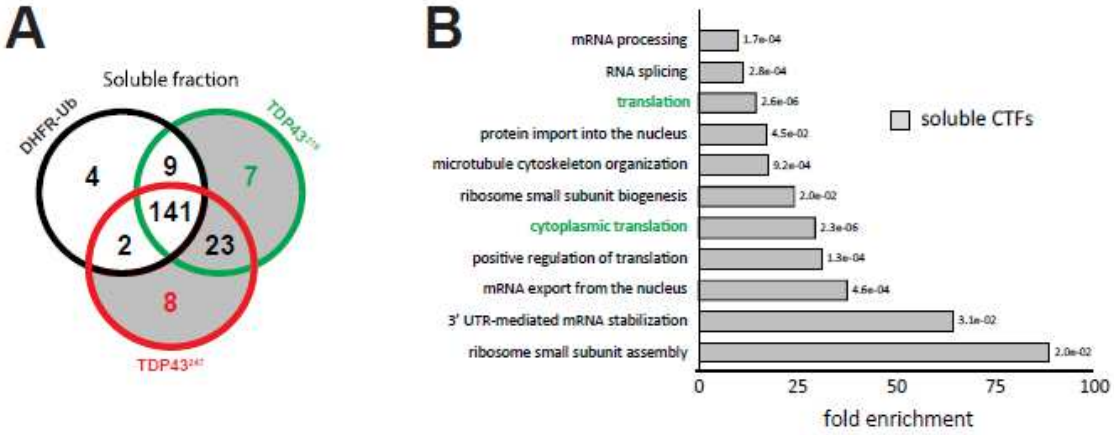
Because CTFs were expressed using URT vectors that co-produce ^{flag}DHFR-Ub (Fig 2A), proteins isolated with ^{flag}DHFR-Ub alone served as controls.

Across both the soluble and insoluble fractions, most proteins were shared among DHFR-Ub, TDP43^{219}, and TDP43^{247} with a minority uniquely associated with individual constructs (Fig 5A, 5D, and Tables S2 and S3). In the soluble fraction, 194 proteins were identified including 4 unique to DHFR-Ub, 7 to TDP43^{219}, and 8 to TDP43^{247} (Fig. 5A and Table S2). The insoluble fraction yielded 478 proteins, with 12 unique to DHFR-Ub, 19 to TDP43^{219}, and 8 to TDP43^{247} (Fig. 5D and Table S3). TDP43-derived peptides were detected in both fractions (three from the soluble fraction and six from the insoluble fraction), whereas none were in DHFR-Ub controls (Fig. 5C and F). Notably, the insoluble fraction included two peptides derived from endogenous TDP43 (TDP43$^{56-79}$ and TDP43$^{84-95}$) (Fig 5F).

To characterize biological processes associated with CTF-specific interactions, we performed gene ontology (GO) enrichment analysis on proteins uniquely associated with CTFs and absent from DHFR-Ub samples. This analysis included 38 proteins from the soluble fraction (Fig. 5A) and 68 from the insoluble fraction (Fig. 5D). Proteins associated with soluble CTFs were enriched for nuclear and post-transcriptional RNA-related processes, including RNA splicing, mRNA processing, mRNA export, and regulation of translation, as well as nuclear transport and select cytoskeletal organization terms (Fig. 5B).

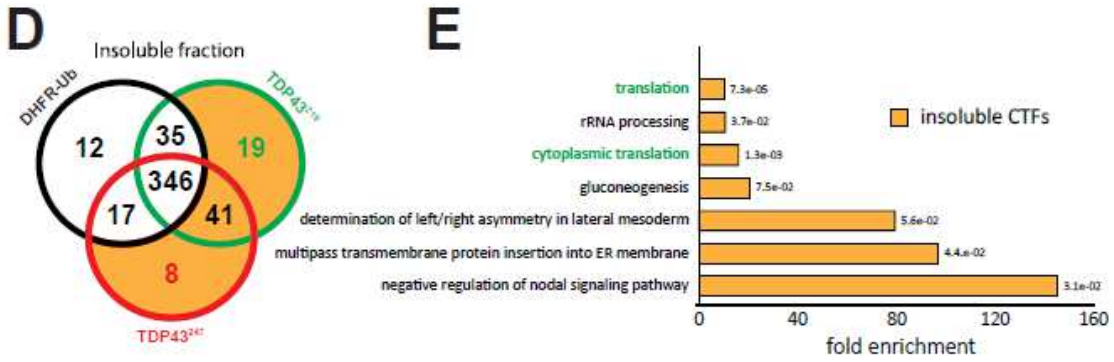
Proteins uniquely associated with insoluble CTFs were also enriched for translation and RNA processing terms, although fewer RNA regulatory categories were represented compared with the soluble fraction. In addition, the insoluble CTF interactome showed enrichment for categories not observed in the soluble fraction, including gluconeogenesis, multipass transmembrane protein insertion into the ER membrane, and developmental signaling terms such

as determination of left/right asymmetry in lateral mesoderm and negative regulation of nodal signaling (Fig. 5E). Together, these analyses indicate that soluble and insoluble TDP43 CTF fractions exhibit overlapping but distinct GO enrichment profiles, reflecting differences in the composition of their associated protein sets.



C

Soluble fraction			
position	peptide	instances	co-IP'ed with
228-251	AFAFVTFADDQIAQSLCGEDLIIK	11	TDP43^{219}
252-263	GISVHISNAEPK	8	TDP43^{219} and TDP43^{247}
276-293	FGGNPGGFGNQGGFGNSR	4	TDP43^{219} and TDP43^{247}



F

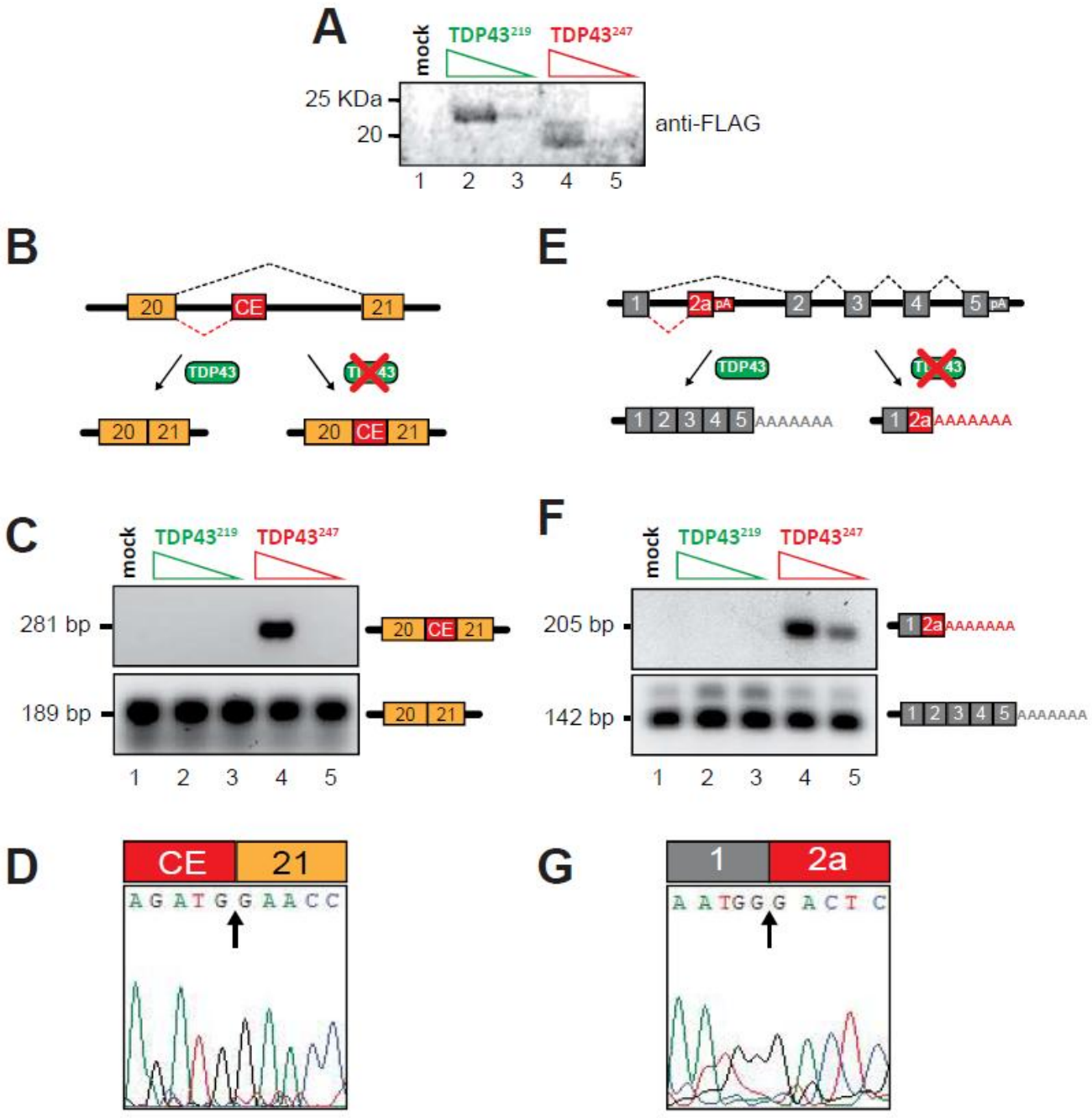
Insoluble fraction			
position	peptide	instances	co-IP'ed with
56-79	LVEGILHAPDAGWGNLVYVVNYPK	2	TDP43^{219}
84-95	KMDETDASSAVK	1	TDP43^{247}
228-251	AFAFVTFADDQIAQSLCGEDLIIK	5	TDP43^{219}
252-263	GISVHISNAEPK	6	TDP43^{219} and TDP43^{247}
276-293	FGGNPGGFGNQGGFGNSR	41	TDP43^{219} and TDP43^{247}
362-408	EPNQAFGSGNNSYSGSNSGAAIGWGSASNAGSGSGFNGGFGSSMDSK	1	TDP43^{247}

Splicing defects

Prior studies have demonstrated that TDP43 binds GU-rich regions within pre-mRNAs to regulate alternative splicing of a broad set of disease-relevant transcripts [53]. Specifically, loss of TDP43 function was shown to result in inclusion of a cryptic exon between exons 20 and 21 of *UNC13A* pre-mRNA, triggering nonsense-mediated decay and depletion of UNC13A protein (Fig. 6B), a key regulator of synaptic vesicle fusion and neurotransmitter release [34]. Similarly, TDP43 binds a GU-rich region adjacent to a cryptic 3′ splice site within *STMN2* pre-mRNA between exons 1 and 2, thereby suppressing inclusion of cryptic exon 2a, which contains a premature stop codon and polyadenylation signal (Fig. 6E). Disruption of this regulatory activity results in production of a truncated transcript and depletion of functional Stathmin-2, a microtubule-associated protein essential for axonal growth and repair [32, 33, 35].

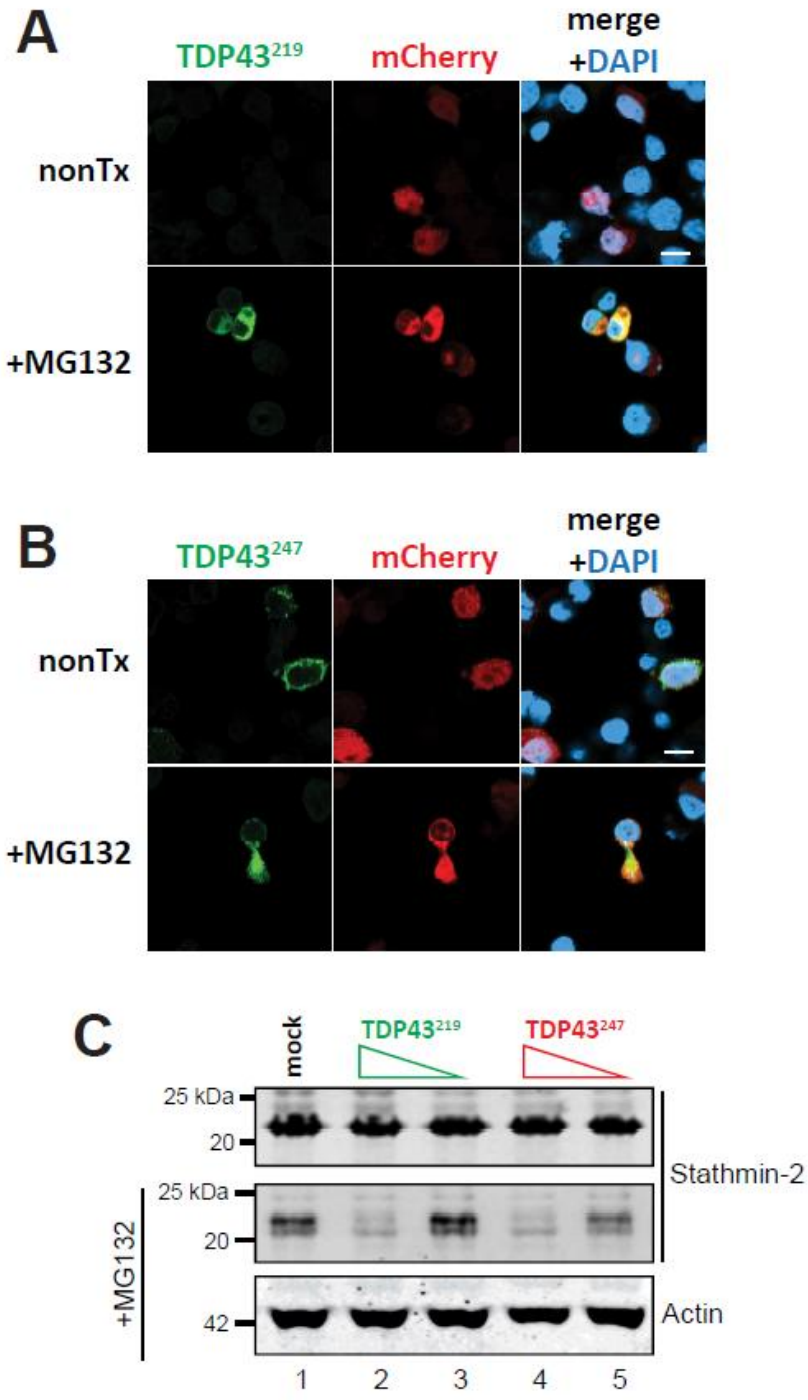
To determine whether TDP43 CTFs alter pre-mRNA splicing of *UNC13A* and *STMN2*, we expressed $TDP43^{219}$ and $TDP43^{247}$ under either the CMV promoter or the higher-expression EF1α promoter to generate graded CTF levels (Fig. 6A) and performed RT-PCR in HEK-293T cells using gene-specific primers. For *UNC13A*, correctly spliced transcripts (exon 20 joined directly to exon 21; 189 bp) were detected under all conditions (Fig. 6C, *lower panel*), whereas cryptic exon-containing transcripts (281 bp) were detected exclusively in cells expressing high levels of the aggregation-prone $TDP43^{247}$ (Fig. 6C, *upper panel, lane 4*). The 281 bp amplicon was gel-purified and validated by Sanger sequencing, confirming inclusion of the predicted cryptic exon and the expected exon junctions (Fig. 6D). Similarly, correctly spliced *STMN2* transcripts (142 bp) were present in all samples (Fig. 6F, *lower panel*), while cryptic exon 2a-containing transcripts (205 bp) were detected only in cells expressing $TDP43^{247}$, with increased

abundance at higher expression levels (Fig. 6F, *lanes 4 vs. 5*). Sanger sequencing verified the exon 1-cryptic exon 2a junction (Fig. 6G). Together, these data show that cryptic exon inclusion in *UNC13A* and *STMN2* is observed specifically under conditions of elevated TDP43^{247}.



To determine whether the RNA splicing defects were accompanied by reduced protein expression, we measured Stathmin-2 levels in SH-SY5Y cells electroporated with URT constructs encoding $TDP43^{219}$ or $TDP43^{247}$ under the control of either the CMV or EF1α promoter. SH-SY5Y cells were selected for these experiments because they express substantially higher basal levels of Stathmin-2 protein than HEK-293T cells, permitting reliable detection of changes at the protein level. As observed previously in neuronal cultures (Fig. 2C-E), Val-$TDP43^{219}$ did not form detectable aggregates in SH-SY5Y cells under basal conditions (Fig. 7A), whereas Val-$TDP43^{247}$ produced readily detectable cytoplasmic aggregates by immunocytochemistry (Fig. 7B). Treatment with the proteasome inhibitor MG132 induced robust aggregation of both Val-$TDP43^{219}$ and Val-$TDP43^{247}$ in electroporated cells (Fig. 7A and B).

Consistent with an aggregate-dependent effect, immunoblot analysis revealed no difference in Stathmin-2 protein levels under basal conditions relative to mock-electroporated controls. In contrast, proteasome inhibition with MG132, which enhanced intracellular CTF accumulation and aggregation (Fig 7A and B), resulted in a marked reduction in Stathmin-2 protein in cells expressing $TDP43^{219}$ or $TDP43^{247}$ (Fig. 7C, *lanes 2 and 4*). This pattern is consistent with a threshold model in which disruption of *STMN2* expression occurs only when aggregate burden exceeds a critical level, paralleling our observation that cryptic exon-containing transcripts were detected predominantly under high-expression conditions driven by the EF1α promoter. Together, these data support a model in which elevated CTF aggregation is associated with reduced Stathmin-2 protein levels.



587

588 Discussion

589 We previously defined distinct degradation profiles for TDP43^{219} and TDP43^{247}, two

590 largely identical, disease-associated C-terminal fragments of TDP43 [30, 31]. In the present

591 study, we selectively manipulated their stability to examine the consequences of their
592 accumulation in the presence of full-length, functional TDP43. This approach allowed us to
593 directly test whether aggregation-prone TDP43 fragments are sufficient to drive disease-relevant
594 phenotypes independently of TDP43 loss-of-function. We show that failure to degrade TDP43
595 CTFs leads to their aggregation and that an elevated aggregate load associated with disruption of
596 RNA processing.

597 Several observations support this conclusion: (1) blocking degradation resulted in robust
598 CTF aggregation; (2) aggregation-prone CTFs induced motor deficits in mice; (3) insoluble
599 CTFs were associated with endogenous full-length TDP43 and other RNA-binding proteins; and
600 (4) a high aggregate burden of CTFs was accompanied by dysregulation of canonical TDP43-
601 dependent splicing targets, including *UNC13A* and *STMN2*, with corresponding reductions in at
602 least Stathmin-2 protein. Importantly, splicing defects scaled with CTF accumulation. Cryptic
603 exon inclusion was most prominent under high-expression conditions driven by the EF1α
604 promoter, which permitted substantial CTF accumulation and aggregation, whereas lower
605 expression conditions produced minimal or undetectable effects. These data indicate that RNA-
606 processing defects emerge once CTF burden surpasses a critical threshold, consistent with a
607 graded, aggregation-linked effect rather than an all-or-none consequence of fragment expression.

608 Collectively, our findings support a model in which disruption of specific PQC pathways,
609 rather than CTF production alone, drives toxicity. Blocking Arg/N-degron-mediated degradation
610 selectively stabilizes the aggregation-prone TDP43^{247}, leading to neuronal aggregation and motor
611 deficits in mice despite intact, endogenous TDP43, consistent with a toxic gain-of-function
612 mechanism. In contrast, TDP43^{219} remains largely non-toxic due to additional BAG6-dependent
613 and N-degron-independent clearance pathways [31]. This multi-layered PQC framework

suggests that neuronal vulnerability reflects both fragment generation and the availability of fragment-specific clearance mechanisms, potentially contributing to selective susceptibility across neuronal populations.

Consistent with this heterogeneity, aggregates were detected in only ~30% of neurons expressing TDP43^{247} (Fig 2C and D), implying that additional clearance pathways limit fragment accumulation in a subset of cells. Although mitotic inhibitors were used in our neural cultures, the presence of non-neuronal cells cannot be excluded. Future studies examining cell type-specific aggregation and clearance will be important for determining whether distinct neural populations harbor protective mechanisms that constrain TDP43^{247} accumulation.

Splicing defects associated with TDP43 dysfunction have most often been attributed to nuclear depletion of full-length TDP43. However, aberrant splicing can also occur in the absence of overt aggregation or nuclear clearance of TDP43 [54], indicating that multiple mechanisms can perturb TDP43-dependent RNA processing. Although prior studies reported that overexpression of TDP43 CTFs did not alter CFTR exon 9 splicing in minigene assays [9, 25], such reporter systems may not capture the selective vulnerability of endogenous cryptic exon repression programs. Whether aggregation-prone CTFs disrupt endogenous targets such as *UNC13A* and *STMN2* under conditions of cytoplasmic accumulation has therefore remained unresolved.

Our data supports an association between CTF aggregation and disruption of endogenous TDP43-dependent splicing, while also highlighting detection constraints across cellular systems. HEK-293T cells, which can be transfected at >90% efficiency, allow robust detection of cryptic exon inclusion by RT-PCR but do not robustly express endogenous Stathmin-2, precluding assessment of protein-level analysis. In contrast, SH-SY5Y cells express Stathmin-2 and allow

637 immunoblot detection, yet electroporation efficiency (~30%) substantially limits transcript-level
638 sensitivity. Thus, absence of detectable cryptic exon inclusion in SH-SY5Y cells likely reflects
639 dilution by non-transfected cells rather than absence of splicing dysregulation. Notably,
640 reductions in Stathmin-2 protein were observed only under conditions that increased CTF load
641 (e.g. EF1α-driven high expression combined with proteasome inhibition), further supporting a
642 burden-dependent effect.

643 Proteomic analyses further support this framework. Soluble TDP43 CTFs were enriched
644 for RNA splicing factors, including HNRPC, PUF60, RBMX, TFP11, and IF4A3 (Table S2),
645 while endogenous full-length TDP43 was detected within insoluble CTF-containing fractions
646 (Fig. 5F). Together, these findings indicate that CTF aggregation alters native TDP43 interaction
647 networks and recruits additional splicing regulators, suggesting that the observed defects reflect
648 disruption of broader RNA-processing complexes rather than impairment of TDP43 alone.

649 These results place our findings in context with prior reports showing that certain CTFs
650 induce toxicity without overt loss of full-length TDP43 [9, 25], underscoring the context
651 dependence of CTF-mediated effects. Consistent with proximity-labeling studies demonstrating
652 that insoluble TDP43^{208} associates with components of the nuclear pore complex and
653 nucleocytoplasmic transport machinery [55], our analyses identified interactions with
654 import/export receptors, nuclear pore-associated proteins, and shuttling RNA-binding proteins
655 (Table S2 and S3). Together, these data support a model in which aggregation-prone TDP43
656 CTFs disrupt TDP43-centered interaction networks and intersect nucleocytoplasmic transport
657 and RNA-processing pathways.

658 Finally, prior studies have implicated mitochondrial dysfunction as a downstream
659 consequence of TDP43 pathology [56-59], including reports that disease-associated CTFs can

localize to damaged mitochondria and engage mitophagy pathways [60]. Although our interactome analysis identified a limited subset of proteins linked to cellular energy metabolism, we did not directly assess mitochondrial localization, bioenergetic function, or mitophagy. Thus, it remains unclear whether these associations reflect direct mitochondrial engagement by insoluble CTFs or secondary effects of aggregation-induced cellular stress. Future studies combining fragment-specific stabilization with direct measurements of mitochondrial morphology, respiration, and quality control will be required to clarify the contribution of mitochondrial dysfunction to TDP43 CTF-mediated toxicity.

Conflicts of Interests

The authors declare no conflicts of interest.

Ethics Declaration

All animal procedures were approved by the Texas Woman's University Institutional Animal Care and Use Committee (IACUC) (Approval No.: 2023-05) and were conducted in accordance with the Public Health Service (PHS) Policy on Humane Care and Use of Laboratory Animals, as administered by the Office of Laboratory Animal Welfare (OLAW). All efforts were made to minimize animal suffering and to reduce the number of animals used.

Acknowledgements

We thank the UT Southwestern Proteomics Core for assistance with LC-MS/MS analysis and data processing. We are grateful to members of the Brower laboratory for technical support and helpful discussions, particularly Stacy Benjamin, Abby Pellacani, and Safi Syed. We also thank Karl Deisseroth for the pAAV-EF1-Cre plasmid (Addgene #55636). Lentiviral packaging services were provided by Applied Biological Materials Inc.

This work was supported by the TWU, NSF-PRIME Program (S.P.), the TWU Project ACCESS Program (W.M.), the TWU Center for Student Research Program (W.M.), the TWU Research Enhancement Program (C.B.), and the National Institute of Neurological Disorders And Stroke of the National Institutes of Health under award number R15NS095317 (C.B.). The content is solely the responsibility of the authors and does not necessarily represent the official views of the National Institutes of Health.

Figure Legends

Figure 1. Two distinct pathways mediate degradation of C-terminal TDP43 fragments. *N-degron-mediated degradation***:** CTFs bearing destabilizing N-terminal residues (e.g., Asp) are arginylated by ATE1, enabling recognition by UBR family N-recognin E3 ligases (UBR1, UBR2, UBR4, UBR5), followed by ubiquitination and proteasomal degradation. *Hydrophobicity-mediated degradation:* CTFs with exposed hydrophobic regions (e.g., $TDP43^{219}$) are also recognized by the BAG6 chaperone complex, which recruits E3 ligases such as RNF126 to facilitate ubiquitination and proteasomal turnover.

Figure 2. TDP43 C-terminal fragments aggregate and induce neuronal toxicity in primary mouse neurons. (A) Schematic of the ubiquitin reference technique (URT), in which cellular deubiquitinases (DUBs) cleave the fusion protein co-translationally to ensure equimolar production of mCherry-Ub and FLAG-tagged CTFs. (B) *top panels*: anti-TDP43 immunoblot analysis of detergent-soluble and -insoluble fractions from cells expressing mCherry-Ub, mCherry-Ub-TDP43^{219}, or mCherry-Ub-TDP43^{247}, in the presence or absence of the proteasome inhibitor MG132. *Bottom panel*: anti-mCherry immunoblot. (C) Representative confocal images of neural cells five days post-lentiviral transduction. Transduced cells are identified by direct mCherry fluorescence (red); CTFs are detected by indirect immunofluorescence using anti-FLAG followed by an Alexa Fluor 488-conjugated secondary antibody (green); nuclei are stained with DAPI (blue). Scale bars, 10 μm. (D) Quantification of the percentage of mCherry-positive neural cells containing detectable TDP43 aggregates (~200 cells per condition). Data were analyzed by one-way ANOVA ($F(2, 588) = 111.47$) followed by Bonferroni post-hoc tests; TDP43^{247}-expressing cells showed increased aggregation compared with TDP43^{219} and mCherry controls (***$p < 0.001$). (E) Aggregate burden following MG132 treatment, showing robust accumulation of both TDP43^{219} and TDP43^{247} upon proteasome inhibition (***$p < 0.001$). (F) An anti-PARP immunoblot indicating PARP cleavage in neural cells expressing TDP43^{219} and TDP43^{247}. Bars represent groups means + SEM.

Figure 3. CTFs of TDP43 induce neuronal pathology and motor deficits in wildtype mice. (A) Longitudinal hindlimb clasping scores were integrated for each mouse as area under the curve (AUC; score × weeks) and are presented as mean ± SEM. Hindlimb clasping was assessed using a standard ordinal neurological scale (0 - 3), where a score of 0 indicates normal outward

724 splaying of the hindlimbs and increasing scores reflect progressive hindlimb retraction (clasping)
725 toward the abdomen, indicative of neurological dysfunction. Data were analyzed by one-way
726 ANOVA ($F(2,27) = 8.172$) followed by Fisher's LSD post hoc tests ($*p < 0.05$). (B) Average
727 time (seconds) required to traverse a 100-cm beam of decreasing width (15, 10, and 6 mm). Data
728 were analyzed by one-way ANOVA (15 mm: $F(2,28) = 23.93$; 10 mm: $F(2,28) = 4.62$; 6 mm:
729 $F(2,28) = 7.95$) followed by Bonferroni post hoc tests ($*p < 0.05$, $**p < 0.01$, $***p < 0.001$). (C)
730 Average number of foot slips during beam traversal at each beam width. Data are presented as
731 +SEM. Data were analyzed by one-way ANOVA (15 mm: $F(2,27) = 8.151$) followed by
732 Bonferroni post hoc tests ($**p < 0.01$).
733
734 **Figure 4. Gait analysis in mice expressing TDP43 CTFs.** (A) Schematic illustrating gait
735 parameters measured 8 months post-infection. (B) No significant differences in forelimb or
736 hindlimb stride width were observed among groups. (C) Toe spread was not significantly altered
737 in forelimb or hindlimb measurements across experimental conditions. (D) Mice expressing
738 $TDP43^{219}$ or $TDP43^{247}$ exhibited significantly reduced forelimb and hindlimb stride length
739 compared with mCherry-expressing controls. Differences between groups were analyzed by one
740 way ANOVA (Hindlimb: $F(2,54) = 7.372$; Forelimb: $F(2,53) = 6.302$) followed by Bonferroni
741 post hoc tests ($*p < 0.05$, $**p < 0.01$).
742
743 **Figure 5. Distinct interactomes and functional enrichments of TDP43 CTFs isolated from**
744 **detergent-soluble and detergent-insoluble fractions.** (A) Venn diagram showing proteins co-
745 immunoprecipitated from detergent-soluble fractions with DHFR-Ub (control), $TDP43^{219}$, or
746 $TDP43^{247}$. Numbers indicate unique and shared interactors identified by LC-MS/MS. Complete

protein lists are provided in Tables S2 and S3. (B) Gene Ontology (GO) Biological Process enrichment analysis of the 38 proteins selectively enriched with soluble CTFs that were not also associated with DHFR-Ub. Shown are significantly enriched biological processes (false discovery rate [FDR] ≤ 0.05). Bars indicate fold enrichment, with representative GO terms annotated alongside their corresponding FDR values. (C) TDP43-derived peptides identified in detergent-soluble fractions, mapped by position within the human TDP43 sequence (Protein ID: Q13148) and by frequency of detection, and classified according to association with $TDP43^{219}$, $TDP43^{247}$, or both. (D) Same as in (A), but for proteins co-immunoprecipitated from detergent-insoluble, urea-solubilized and renatured fractions. (E) Same analysis as in (B), performed on the 68 proteins selectively enriched with insoluble CTFs that were also not associated with DHFR-Ub. (F) Same as in (C), but for detergent-insoluble fractions.

Figure 6. Aggregation-prone TDP43 C-terminal fragments induce cryptic exon inclusion in *UNC13A* and *STMN2* transcripts. (A) Immunoblot of HEK-293T cells transfected with FLAG-tagged $TDP43^{219}$ or $TDP43^{247}$ under either CMV (moderate expression) or EF1α (high expression) promoters to generate graded fragment accumulation. Anti-FLAG immunoblot confirms relative expression levels across conditions. (B) Schematic of *UNC13A* pre-mRNA splicing. In the presence of functional nuclear TDP43, the cryptic exon (CE) between exons 20 and 21 is repressed, yielding the canonical exon 20-21 junction. Loss or impairment of TDP43 function permits CE inclusion. (C) RT-PCR analysis of *UNC13A* splicing. The upper panel detects cryptic exon inclusion (281 bp product spanning the CE-exon 21 junction), whereas the lower panel detects canonical splicing (189 bp product spanning the exon 20-21 junction). Increased CE inclusion is observed under conditions of high $TDP43^{247}$ expression. (D)

Validation of *UNC13A* cryptic exon inclusion by Sanger sequencing. The 281 bp RT-PCR product was gel-purified and sequenced, confirming the precise CE-exon 21 junction. Representative chromatogram is shown. (E) Schematic of *STMN2* pre-mRNA splicing. Functional TDP43 suppresses inclusion of cryptic exon 2a located between exons 1 and 2. Impaired TDP43 activity results in exon 2a inclusion and premature polyadenylation. (F) RT-PCR analysis of *STMN2* splicing. The upper panel detects cryptic exon inclusion (205 bp product spanning exon 1-2a), and the lower panel detects canonical splicing (142 bp product spanning exons 2-3). Cryptic exon inclusion is most prominent in cells expressing high levels of aggregation-prone $TDP43^{247}$. (G) Validation of *STMN2* cryptic exon inclusion by Sanger sequencing. The 205 bp RT-PCR product was gel-purified and sequenced to confirm the exon 1-2a junction. Representative chromatogram is shown.

Figure 7. High aggregate burden of TDP43 C-terminal fragments reduces Stathmin-2 levels. (A) Representative confocal images of SH-SY5Y cells expressing $TDP43^{219}$ (green) together with mCherry (red) under basal conditions (nonTx) or following proteasome inhibition with MG132. Nuclei are counterstained with DAPI (blue). (B) Same as in (A) except with $TDP43^{247}$. Scale bars, 10 μm. (C) Representative immunoblot of SH-SY5Y cell lysates expressing $TDP43^{219}$ or $TDP43^{247}$. *upper panel*: Stathmin-2 in non-Tx cells; *middle panel*: Stathmin-2 in MG132-treated cells; *lower panel*: actin (loading control).

Figure S1. Stereotaxic delivery of TDP43 C-terminal fragments to the primary motor cortex of wild-type mice. (A) Schematic illustrating unilateral stereotaxic injection of lentiviral constructs into the primary motor cortex of the right hemisphere. Wild-type mice received

lentivirus encoding mCherry-Ub alone, mCherry-Ub-Val-TDP43^{219} or mCherry-Ub-Val-TDP43^{247}, enabling localized expression of TDP43 C-terminal fragments in a TDP43-competent background. (B) Representative coronal brain sections from a non-treated mouse and a lentivirus-injected mouse stained with anti-GFAP to verify targeting of the primary motor cortex. Sustained astrocyte reactivity was observed at the injection site up to 10 months post-surgery (arrow). (C) Immunohistochemical analysis of the motor cortex 10 months post-injection showing perinuclear aggregates of TDP43^{247} (arrows). CTFs were detected by indirect immunofluorescence using anti-FLAG followed by an Alexa Fluor 488-conjugated secondary antibody (green); nuclei were counterstained with DAPI (blue). Scale bars, 20 μm.

Figure S2. Longitudinal body weight measurements of mice expressing mCherry, TDP43^{219}, or TDP43^{247}. Total body weight (gm) was recorded at 0, 5, and 10 months post-surgery following stereotaxic delivery of the indicated constructs. Box plots show median, interquartile range, and individual data points for each group, with whiskers indicating range. The average weight in each group is indicated by an "x". No significant differences were detected between groups.

Figure S3. Survival of mice expressing mCherry, TDP43^{219}, or TDP43^{247} following stereotaxic injection. Kaplan-Meier survival analysis of wild-type mice following stereotaxic injection of lentiviral constructs encoding mCherry-Ub alone, mCherry-Ub-Val-TDP43^{219} or mCherry-Ub-Val-TDP43^{247} into the primary motor cortex. Mice were monitored for up to ~300 days post-surgery.

Figure S4. Motor performance of mice expressing mCherry, TDP43^{219}, or TDP43^{247} assessed by accelerating rotarod. Performance ratios were measured longitudinally from 1 to 10 months post-surgery and normalized to each animal's baseline performance. Bars represent mean + SEM for each group at the indicated time points. No significant differences were detected between groups. The performance ratio was calculated as the latency to fall from the rotarod relative to the mCherry-Ub control group, which was set to 1.

Figure S5. Longitudinal hindlimb clasping in mice expressing TDP43 C-terminal fragments. Hindlimb clasping was assessed longitudinally for up to 30 weeks post-surgery in mice expressing TDP43^{219} or TDP43^{247} and compared independently to wild-type (WT) controls. Clasping was scored using a standard ordinal neurological scale (0 - 3), where a score of 0 indicates normal outward hindlimb splaying and higher scores reflect progressive hindlimb retraction toward the abdomen, indicative of neurological impairment. (A) WT vs. TDP43^{219}. No significant differences in hindlimb clasping were observed over time. (B) WT vs. TDP43^{247}. Mice expressing TDP43^{247} exhibited elevated hindlimb clasping scores relative to WT controls across the study period. Data are presented as mean ± SEM.

References

1. Robberecht, W. and T. Philips, *The changing scene of amyotrophic lateral sclerosis.* Nature Reviews Neuroscience, 2013. **14**(4): p. 248-264.
2. Neumann, M., et al., *Ubiquitinated TDP-43 in frontotemporal lobar degeneration and amyotrophic lateral sclerosis.* Science, 2006. **314**(5796): p. 130-3.
3. Budini, M., et al., *Cellular model of TAR DNA-binding protein 43 (TDP-43) aggregation based on its C-terminal Gln/Asn-rich region.* J Biol Chem, 2012. **287**(10): p. 7512-25.
4. D'Ambrogio, A., et al., *Functional mapping of the interaction between TDP-43 and hnRNP A2 in vivo.* Nucleic Acids Res, 2009. **37**(12): p. 4116-26.
5. Romano, M., F. Feiguin, and E. Buratti, *Drosophila Answers to TDP-43 Proteinopathies.* J Amino Acids, 2012. **2012**: p. 356081.

6. Kametani, F., et al., *Mass spectrometric analysis of accumulated TDP-43 in amyotrophic lateral sclerosis brains.* Sci Rep, 2016. **6**: p. 23281.
7. Kitamura, A., et al., *Interaction of RNA with a C-terminal fragment of the amyotrophic lateral sclerosis-associated TDP43 reduces cytotoxicity.* Sci Rep, 2016. **6**: p. 19230.
8. Nonaka, T., et al., *Phosphorylated and ubiquitinated TDP-43 pathological inclusions in ALS and FTLD-U are recapitulated in SH-SY5Y cells.* FEBS Lett, 2009. **583**(2): p. 394-400.
9. Zhang, Y.J., et al., *Aberrant cleavage of TDP-43 enhances aggregation and cellular toxicity.* Proc Natl Acad Sci U S A, 2009. **106**(18): p. 7607-12.
10. Aulas, A. and C. Vande Velde, *Alterations in stress granule dynamics driven by TDP-43 and FUS: a link to pathological inclusions in ALS?* Front Cell Neurosci, 2015. **9**: p. 423.
11. Ling, S.C., M. Polymenidou, and D.W. Cleveland, *Converging mechanisms in ALS and FTD: disrupted RNA and protein homeostasis.* Neuron, 2013. **79**(3): p. 416-38.
12. Tan, Q., et al., *Extensive cryptic splicing upon loss of RBM17 and TDP43 in neurodegeneration models.* Hum Mol Genet, 2016. **25**(23): p. 5083-5093.
13. Ou, S.H., et al., *Cloning and characterization of a novel cellular protein, TDP-43, that binds to human immunodeficiency virus type 1 TAR DNA sequence motifs.* J Virol, 1995. **69**(6): p. 3584-96.
14. Li, Y.R., et al., *Stress granules as crucibles of ALS pathogenesis.* J Cell Biol, 2013. **201**(3): p. 361-72.
15. Wu, L.S., et al., *TDP-43, a neuro-pathosignature factor, is essential for early mouse embryogenesis.* Genesis, 2010. **48**(1): p. 56-62.
16. Ayala, Y.M., T. Misteli, and F.E. Baralle, *TDP-43 regulates retinoblastoma protein phosphorylation through the repression of cyclin-dependent kinase 6 expression.* Proc Natl Acad Sci U S A, 2008. **105**(10): p. 3785-9.
17. Bose, J.K., et al., *TDP-43 overexpression enhances exon 7 inclusion during the survival of motor neuron pre-mRNA splicing.* J Biol Chem, 2008. **283**(43): p. 28852-9.
18. Iguchi, Y., et al., *TDP-43 depletion induces neuronal cell damage through dysregulation of Rho family GTPases.* J Biol Chem, 2009. **284**(33): p. 22059-66.
19. Ling, J.P., et al., *TDP-43 repression of nonconserved cryptic exons is compromised in ALS-FTD.* Science, 2015. **349**(6248): p. 650-5.
20. Amlie-Wolf, A., et al., *Transcriptomic Changes Due to Cytoplasmic TDP-43 Expression Reveal Dysregulation of Histone Transcripts and Nuclear Chromatin.* PLoS One, 2015. **10**(10): p. e0141836.
21. Fiesel, F.C., et al., *TDP-43 knockdown impairs neurite outgrowth dependent on its target histone deacetylase 6.* Mol Neurodegener, 2011. **6**: p. 64.
22. Nehls, J., et al., *HIV-1 replication in human immune cells is independent of TAR DNA binding protein 43 (TDP-43) expression.* PLoS One, 2014. **9**(8): p. e105478.
23. Hergesheimer, R.C., et al., *The debated toxic role of aggregated TDP-43 in amyotrophic lateral sclerosis: a resolution in sight?* Brain, 2019. **142**(5): p. 1176-1194.
24. Li, Q., et al., *The cleavage pattern of TDP-43 determines its rate of clearance and cytotoxicity.* Nat Commun, 2015. **6**: p. 6183.
25. Nonaka, T., et al., *Truncation and pathogenic mutations facilitate the formation of intracellular aggregates of TDP-43.* Hum Mol Genet, 2009. **18**(18): p. 3353-64.

26. Igaz, L.M., et al., *Expression of TDP-43 C-terminal Fragments in Vitro Recapitulates Pathological Features of TDP-43 Proteinopathies.* J Biol Chem, 2009. **284**(13): p. 8516-24.
27. Zhang, Y.J., et al., *Progranulin mediates caspase-dependent cleavage of TAR DNA binding protein-43.* J Neurosci, 2007. **27**(39): p. 10530-4.
28. Yamashita, T., et al., *A role for calpain-dependent cleavage of TDP-43 in amyotrophic lateral sclerosis pathology.* Nat Commun, 2012. **3**: p. 1307.
29. Brower, C.S., K.I. Piatkov, and A. Varshavsky, *Neurodegeneration-associated protein fragments as short-lived substrates of the N-end rule pathway.* Mol Cell, 2013. **50**(2): p. 161-71.
30. Kasu, Y.A.T., et al., *The N-termini of TAR DNA-binding protein-43 (TDP43) C-terminal fragments influence degradation, aggregation propensity and morphology.* Mol Cell Biol, 2018. **38**(19): p. e00243-18.
31. Kasu, Y.A.T., et al., *BAG6 prevents the aggregation of neurodegeneration-associated fragments of TDP43.* iScience, 2022. **25**(5): p. 104273.
32. Melamed, Z., et al., *Premature polyadenylation-mediated loss of stathmin-2 is a hallmark of TDP-43-dependent neurodegeneration.* Nat Neurosci, 2019. **22**(2): p. 180-190.
33. Klim, J.R., et al., *ALS-implicated protein TDP-43 sustains levels of STMN2, a mediator of motor neuron growth and repair.* Nat Neurosci, 2019. **22**(2): p. 167-179.
34. Brown, A.L., et al., *TDP-43 loss and ALS-risk SNPs drive mis-splicing and depletion of UNC13A.* Nature, 2022. **603**(7899): p. 131-137.
35. Baughn, M.W., et al., *Mechanism of STMN2 cryptic splice-polyadenylation and its correction for TDP-43 proteinopathies.* Science, 2023. **379**(6637): p. 1140-1149.
36. Fenno, L.E., et al., *Targeting cells with single vectors using multiple-feature Boolean logic.* Nat Methods, 2014. **11**(7): p. 763-72.
37. Deitch, J.S., et al., *Phenotype of transgenic mice carrying a very low copy number of the mutant human G93A superoxide dismutase-1 gene associated with amyotrophic lateral sclerosis.* PLoS One, 2014. **9**(6): p. e99879.
38. Powell, E., et al., *The splay angle: A new measure for assessing neuromuscular dysfunction in rats.* Physiol Behav, 1999. **67**(5): p. 819-21.
39. Trudgian, D.C. and H. Mirzaei, *Cloud CPFP: A Shotgun Proteomics Data Analysis Pipeline Using Cloud and High Performance Computing.* Journal of Proteome Research, 2012. **11**(12): p. 6282-6290.
40. Trudgian, D.C., et al., *CPFP: a central proteomics facilities pipeline.* Bioinformatics, 2010. **26**(8): p. 1131-1132.
41. Craig, R. and R.C. Beavis, *TANDEM: matching proteins with tandem mass spectra.* Bioinformatics, 2004. **20**(9): p. 1466-1467.
42. Geer, L.Y., et al., *Open Mass Spectrometry Search Algorithm.* Journal of Proteome Research, 2004. **3**(5): p. 958-964.
43. Elias, J.E. and S.P. Gygi, *Target-decoy search strategy for increased confidence in large-scale protein identifications by mass spectrometry.* Nature Methods, 2007. **4**(3): p. 207-214.
44. Trudgian, D.C., et al., *Comparative evaluation of label-free SINQ normalized spectral index quantitation in the central proteomics facilities pipeline.* PROTEOMICS, 2011. **11**(14): p. 2790-2797.

45. Sherman, B.T., et al., *DAVID: a web server for functional enrichment analysis and functional annotation of gene lists (2021 update).* Nucleic Acids Res, 2022. **50**(W1): p. W216-w221.
46. Braak, H., et al., *Amyotrophic lateral sclerosis: dash-like accumulation of phosphorylated TDP-43 in somatodendritic and axonal compartments of somatomotor neurons of the lower brainstem and spinal cord.* Acta Neuropathol, 2010. **120**(1): p. 67-74.
47. Boulares, H.A., et al., *Role of poly(ADP-ribose) polymerase (PARP) cleavage in apoptosis.* J. Biol. Chem., 1999. **274**: p. 22932-22940.
48. Carter, R.J., J. Morton, and S.B. Dunnett, *Motor coordination and balance in rodents.* Curr Protoc Neurosci, 2001. **Chapter 8**: p. Unit 8.12.
49. Beloozerova, I.N., et al., *Differences in movement mechanics, electromyographic, and motor cortex activity between accurate and nonaccurate stepping.* J Neurophysiol, 2010. **103**(4): p. 2285-300.
50. Farrell, B.J., et al., *Accurate stepping on a narrow path: mechanics, EMG, and motor cortex activity in the cat.* J Neurophysiol, 2015. **114**(5): p. 2682-702.
51. Luong, T.N., et al., *Assessment of motor balance and coordination in mice using the balance beam.* J Vis Exp, 2011(49).
52. Freibaum, B.D., et al., *Global analysis of TDP-43 interacting proteins reveals strong association with RNA splicing and translation machinery.* J Proteome Res, 2010. **9**(2): p. 1104-20.
53. Koike, Y., *Molecular mechanisms linking loss of TDP-43 function to amyotrophic lateral sclerosis/frontotemporal dementia-related genes.* Neurosci Res, 2024. **208**: p. 1-7.
54. Arnold, E.S., et al., *ALS-linked TDP-43 mutations produce aberrant RNA splicing and adult-onset motor neuron disease without aggregation or loss of nuclear TDP-43.* Proc Natl Acad Sci U S A, 2013. **110**(8): p. E736-45.
55. Chou, C.C., et al., *TDP-43 pathology disrupts nuclear pore complexes and nucleocytoplasmic transport in ALS/FTD.* Nat Neurosci, 2018. **21**(2): p. 228-239.
56. Wang, W., et al., *The inhibition of TDP-43 mitochondrial localization blocks its neuronal toxicity.* Nat Med, 2016. **22**(8): p. 869-78.
57. Wang, P., et al., *TDP-43 induces mitochondrial damage and activates the mitochondrial unfolded protein response.* PLoS Genet, 2019. **15**(5): p. e1007947.
58. Yu, C.H., et al., *TDP-43 Triggers Mitochondrial DNA Release via mPTP to Activate cGAS/STING in ALS.* Cell, 2020. **183**(3): p. 636-649.e18.
59. Zuo, X., et al., *TDP-43 aggregation induced by oxidative stress causes global mitochondrial imbalance in ALS.* Nat Struct Mol Biol, 2021. **28**(2): p. 132-142.
60. Jun, M.H., et al., *Nonmuscle myosin IIB regulates Parkin-mediated mitophagy associated with amyotrophic lateral sclerosis-linked TDP-43.* Cell Death Dis, 2020. **11**(11): p. 952.

Supplementary Files

This is a list of supplementary files associated with this preprint. Click to download.

- FigS2mouseweight.tif
- TableS1plasmidsandoligos.docx
- TableS2ProteinsinteractingwithsolubleCTFs.xlsx
- TableS3ProteinsinteracingwithinsoloubleCTFs.xlsx
- FigS5hindlimbclasping.tif
- FigS3survival.tif
- FigS4Rotarod.tif
- FigS1stereotaxicsurgery.tif
- Uncroppedgelsandblots.pdf